

MECHANICAL PROPERTIES OF PHOTOMULTIPLIER TUBE
GLASSES FOR NEUTRINO DETECTION

BY

KAMERON CHAMBLISS

A THESIS
SUBMITTED TO THE FACULTY OF

ALFRED UNIVERSITY

IN PARTIAL FULFILLMENT OF THE REQUIREMENTS
FOR THE DEGREE OF

MASTER OF SCIENCE

IN

MATERIALS SCIENCE AND ENGINEERING

ALFRED, NEW YORK

FEBRUARY, 2014

Alfred University theses are copyright protected and may be used for education or personal research only. Reproduction or distribution in part or whole is prohibited without written permission from the author.

Signature page may be viewed at Scholes Library, New York State College of Ceramics, Alfred University, Alfred, New York.

MECHANICAL PROPERTIES OF PHOTOMULTIPLIER TUBE
GLASSES FOR NEUTRINO DETECTION

BY

KAMERON CHAMBLISS

B.S. ALFRED UNIVERSITY (2010)

SIGNATURE OF AUTHOR _____ (Signature on File)

APPROVED BY _____ (Signature on File)

S.K. SUNDARAM, ADVISOR

(Signature on File)

MATTHEW M. HALL, ADVISORY COMMITTEE

(Signature on File)

WILLIAM C. LACOURSE, ADVISORY COMMITTEE

(Signature on File)

CHAIR, ORAL THESIS DEFENSE

ACCEPTED BY _____ (Signature on File)

DOREEN D. EDWARDS, DEAN
KAZUO INAMORI SCHOOL OF ENGINEERING

ACKNOWLEDGEMENTS

I would like to thank the following colleagues for their direction, and support throughout the duration of my graduate studies:

- Dr. S.K. Sundaram, my advisor, for his support and direction throughout my time as a graduate student.
- Dr. Hall and Dr. LaCourse, my thesis committee members, whose inputs were essential to my success.
- Brookhaven National Laboratory under the Long Baseline Neutrino Experiment, especially Dr. Milind Diwan and Mr. Rahul Sharma.
- Alfred University Athletic Department, Brian Striker, Ross Munson, and Jeff Grover who have served as coaches, mentors, and friends.
- Dr. Wallace Leigh, Matt Degges, Angus Powers, Shaun Griffiths, Jeff Roland, Ish Szabo, John Rich, Ruhil Dongol, Dan Steere, Jim Thiebaud, Gerry Wynick, Libby Tsibulsky, Sam Burlingame, Brynja Seagren, and David Luke, each for their contributions at various stages of this project.

Finally, I would like to thank my parents for the support they have always given me, no matter what.

TABLE OF CONTENTS

	Page
Acknowledgements.....	iii
Table of Contents.....	iv
List of Tables.....	vi
List of Figures.....	vii
Abstract.....	ix
I. INTRODUCTION.....	1
II. LITERATURE REVIEW.....	4
A. Glass Strength and Flaw Contribution.....	4
B. Ion Exchange and Diffusion.....	5
C. Fatigue and Lifetime Predictability.....	6
III. EXPERIMENTAL PROCEDURE, PART 1: ION EXCHANGE.....	9
A. Glass Composition Properties Examined.....	9
1. Glass Compositions.....	9
2. Differential Scanning Calorimetry.....	9
B. Sample Preparation.....	10
1. Rod Samples.....	10
2. Disc Samples.....	11
C. Sodium-Potassium Ion Exchange.....	12
D. Evaluating K ⁺ Exchange Depth.....	12
E. Flexural Strength Measurement.....	13
F. Surface Hardness.....	15
G. UV-Vis Spectroscopy.....	15
IV. EXPERIMENTAL PROCEDURE, PART 2: CRACK VELOCITY.....	16
A. Residual Stress Analysis.....	16
B. Pressure Testing.....	16
C. Crack Velocity Measurement.....	17
D. 3-D Modeling and Curvature Corrections.....	18
V. RESULTS.....	21
A. Differential Scanning Calorimetry.....	21
B. Depth and Profile of K ⁺ Exchange.....	22
C. Flexural Strength.....	25

D. Surface Hardness	28
E. UV-Vis Spectroscopy	29
F. Crack Velocity	31
VI. DISCUSSION	33
A. Ion Exchange Effects on Properties.....	33
1. Flexural Strength	33
2. Indentation Hardness	34
3. Absorbance	34
B. Crack Velocity and Modeling.....	35
VII. SUMMARY AND CONCLUSIONS.....	39
A. Ion Exchange	39
B. Crack Velocity.....	39
VIII. FUTURE WORK	40
IX. REFERENCES	41
X. APPENDIX	45

LIST OF TABLES

	Page
Table I. Nominal Composition Ranges for Vendor Glasses in Weight Percent.....	9
Table II. Predicted Glass Properties for the Given Compositions, Acquired from SciGlass Database.....	9
Table III. Summary of Ion Exchange Profile Results	25
Table IV. Average Modulus of Rupture and Standard Deviation for Vendor Glasses	25
Table V. Summary of Weibull Modulus and Characteristic Strength Results	27
Table VI. Summary of Crack Velocity Data	32
Table VII. Terminal Crack Velocities for Various Reference Glasses ³⁰	36
Table VIII. Crack Velocities Measured in TA3522 After Curvature Correction	37
Table IX. Sample Calculation of Crack Velocity.....	45

LIST OF FIGURES

	Page
Figure 1. Simplified schematic of the stuffing effect observed in low temperature K^+ for Na^+ ion exchange.	5
Figure 2. Artists Jeff Rowland (left) and Shaun Griffiths (right) in the hot glass shop pulling cane from one of the vendor glasses.	11
Figure 3. Diagram of microprobe mapping. The gray area represents the glass sample and the white represents the epoxy mount. The vertical lines indicate paths along which measurements were conducted.	13
Figure 4. Schematic of 4-point bend testing apparatus with important elements and axes labeled.	14
Figure 5. Example of a single frame used for crack measurement, the bulb is being viewed from the top down. Cracks indicated with red are being measured in the current frame in the direction of the arrow. Measurements have been completed on cracks indicated in blue.	18
Figure 6. A top-down view of the bulb model, each line segment represents a measurement point along the crack path, relative to the central peak of the bulb.	19
Figure 7. In a rotated view of the bulb model, the segments from Figure 6 are visible, in dark gray, connected at their ends by the 2-dimensional representation of the crack path. The light gray arc below represents the intersection of the projection of the 2-D path and the bulb surface.	20
Figure 8. Heat flow vs. temperature curve of Vendor 1 composition using a heating rate of $10^{\circ}C$ per minute with T_g estimated at $510^{\circ}C$	21
Figure 9. Heat flow vs. temperature curve of Vendor 2 composition using a heating rate of $10^{\circ}C$ per minute with T_g estimated at $540^{\circ}C$	22
Figure 10. Exchange profile of Vendor 1 glass treated at $470^{\circ}C$ for 24 hours.	23
Figure 11. Exchange profile of Vendor 1 glass treated at $480^{\circ}C$ for 24 hours.	23
Figure 12. Exchange profile of Vendor 2 glass treated at $470^{\circ}C$ for 24 hours.	24
Figure 13. Exchange profile of Vendor 2 glass treated at $480^{\circ}C$ for 24 hours.	24

Figure 14. Weibull plot of 4-point bend strength of Vendor 1 glass at various exchange treatments.....	26
Figure 15. Weibull plot of 4-point bend strength of Vendor 2 glass rods at various exchange treatments.....	27
Figure 16. Vickers Hardness of Vendor 1 glass before and after ion exchange.	28
Figure 17. Vickers Hardness of Vendor 2 glass before and after ion exchange.	29
Figure 18. Normalized absorbance of light between 350 and 500 nm wavelengths of Vendor 1 glass samples "A" and "B" before and after exchange.	30
Figure 19. Normalized absorbance of light between 350 and 500 nm wavelengths of Vendor 2 glass samples "A" and "B" before and after exchange.	30
Figure 20. Scatter plot of average crack velocity against external pressure at failure for each bulb using each of the two methods of measurement.....	32
Figure 21. Individual frame of video showing the location of cracks measured on PMT TA3522.	37
Figure 22. CAD model of a 10-inch PMT showing the maximum principal stresses under uniform hydrostatic pressure.....	38

ABSTRACT

This thesis focuses on various mechanical properties affecting the performance of two vendor-supplied glasses currently used for photomultiplier tubes (PMTs) with the specific objective of improving these properties using chemical (potassium-sodium ion exchange) strengthening. The results show that a 46% increase in MOR with one vendor glass, and a 57% increase in the other, can be produced. The results also show narrowing of the MOR distributions as indicated by an increased Weibull modulus. The additional processing that leads to these improvements, along with increases in surface hardness, had no negative effects on the light absorbance over the wavelengths of interest. These findings suggest that the strengthening process could be optimized to produce even greater strengths and better resiliency of the PMTs in service.

INTRODUCTION

Solar neutrino research is an important area of particle physics that helps the scientific community to answer fundamental questions about astrophysical events such as supernovas and to confirm hypotheses about natural processes that occur inside the sun. The sun constantly produces neutrinos via the following reaction, nuclear fusion:



where $4p$ is four protons or hydrogen nuclei, e^+ are positively charged electrons, and ν_e are electron neutrinos, one of three types of neutrino. This reaction also produces large amounts of energy which reach the earth in the form of sunlight¹. One of the first experiments designed to detect neutrinos on earth was the Homestake Solar Neutrino Observatory chlorine detector in the Homestake Gold Mine in Lead, SD. This experiment used a large tank of C_2Cl_4 cleaning solution and measured the interactions of neutrinos with the solution via creation of radioactive argon atoms². The Homestake detector experiment discovered a three to one discrepancy between the number of neutrino interactions in theoretical model of neutrino production and those observed in the experimental results. This discrepancy became known as the Solar Neutrino Problem. The problem was not solved until 2001 when a team of researchers at the Sudbury Neutrino Observatory³ (SNO) showed that two thirds of the electron neutrinos created in the sun changed into muon and tau neutrinos by the time they reached earth and were not able to be detected by previous experiments¹.

The SNO detector is one of a newer generation of detectors using large volumes of water and large arrays of photomultiplier tubes (PMTs) to monitor neutrino activity including the Super-Kamiokande (Super-K) detector⁴, the Hyper-Kamiokande (Hyper-K) project⁵, and the water Cherenkov detector option for the Long-Baseline Neutrino Experiment (LBNE)⁶ that is being managed by the Fermi Laboratory and Brookhaven National Laboratory (BNL).

Photomultiplier tubes are essential components for maintaining these experiments successfully and their properties and limits must be explored to ensure survival within the experimental environment. The PMTs are exposed to large hydrostatic pressures during

prolonged contact with high purity water. The detector proposed for the LBNE would house PMTs at depths of up to 80 meters, creating external hydrostatic pressures of approximately 890 kPa, or 129 psi⁷. The water purification system will be designed based on knowledge of similar water Cherenkov detectors⁶, where cycling ultra-pure water in the detector ranged in resistivity from 11 to 18.24 MΩ-cm, nearing the theoretical limit⁴. The Hyper-K requirements are similar to LBNE except for the depth, which is currently designed to be about 40 meters⁵, which correlates to an external pressure of approximately 493 kPa.

Sustained PMT performance over extended time periods, a proposed 20 year lifetime for the LBNE, is required to protect the light-sensing devices. One primary issue facing the long-term success of these experiments is structural failure of the PMTs, which could potentially lead to catastrophic cascade failures in the large PMT arrays, especially when the shockwave from a single bulb failure is intense enough to trigger failure in neighboring PMT bulbs. Such failures can disrupt and potentially end long-term experiments before their designed conclusions. Individual bulb failures can result from a number of different factors affecting performance, including bulb shape, thickness of the glass, surface or bulk flaws, stress corrosion, residual stresses from processing, and extended exposure to the environmental conditions of neutrino detection. The crack velocity, and subsequent force generated in a failing PMT bulb, affects the shape and the intensity of the resulting shockwave, making it an important characteristic to understand regarding these failures⁸.

In order to provide a better understanding of the mechanical properties and long term performance of the PMTs in the LBNE project, this thesis endeavors to characterize surface and bulk properties of two vendor-supplied glass compositions used specifically for this application. The strength characteristics (MOR and Weibull constants) were measured for the first time. In addition, an effort was made to improve the strength of these glasses via ion exchange.

The main objectives of the current work were:

1. To investigate the bulk as well as surface mechanical properties of these glass compositions used in neutrino detection experiments.

2. To attempt to improve these properties through ion exchange treatment of the glasses.
3. To correlate those improvements in mechanical properties to the *in situ* reliability of PMTs and provide a basis for lifetime prediction.

LITERATURE REVIEW

A. Glass Strength and Flaw Contribution

The stress required to cause failure in a theoretically perfect brittle solid, such as a glass, is equal to the stress required to break the bonds holding the solid together, and is given by the Orowan expression⁹:

$$\sigma_m = \sqrt{\frac{\gamma_f E}{a_0}} \quad (2)$$

where σ_m is the maximum stress at failure, γ_f is the interfacial surface energy for a pristine surface, E is Young's Modulus, and a_0 is the interatomic separation distance. This equation estimates that the strength of perfect silicate glasses should theoretically reach as high 14-35 GPa¹⁰ and anywhere between 1 and 100 GPa for glass of any composition¹¹.

The production of glass pieces is an energy-intensive thermal process and strength-limiting defects are introduced during different processing steps. Flaws can be introduced during production by contact with a mold surface, any shaping or handling of a piece after cooling, as well as post production consumer use. Inglis was the first to suggest that flaws in the glass act as stress concentrators¹². These flaws control the failure behavior and limit the strength of a piece to a level far below the theoretical values. Later, Griffith showed that a preexisting flaw must exceed a critical length at a given stress before it will propagate into a fracture, in the form of the Griffith equation:

$$\sigma_f = [\sigma_a]_{failure} = \sqrt{\frac{2\gamma_f E}{\pi c^*}} \quad (3)$$

where σ_f is the maximum stress at failure, γ_f is the interfacial surface energy, E is the Young's Modulus, and c^* is the critical flaw length. In a sample featuring multiple defects, fracture will initiate at the most severe flaw, as determined by its shape, size, and location, these are called the Griffith flaws.

Scientific literature contains numerous techniques to improve the strength and toughness of glasses, including acid etching¹³, flame polishing¹⁴, thermal tempering¹⁵, ion exchange¹⁶, surface crystallization¹⁷, and glazing¹⁸. In acid etching and flame polishing,

surfaces are treated in order to reduce the severity of existing flaws. In thermal tempering, ion exchange, surface crystallization, and glazing, the primary mechanism of strengthening is creation of a compression layer on the surface of the glass. In order to cause failure at a given flaw, the tensile force must overcome the compressive force acting in that region in order to cause propagation and lead to failure.

B. Ion Exchange and Diffusion

This thesis specifically explores an ion exchange technique using immersion in a molten potassium nitrate (KNO_3) bath at appropriate temperature to improve the strength of PMT glasses. The driving mechanism for strengthening in this process is ionic substitution. Smaller alkali ions in a glass matrix, such as sodium, can be substituted for slightly larger alkali ions, like potassium, through ionic inter-diffusion at a temperature below the glass transition. Compressive stresses are formed on the exposed surface of the glass, where the exchange occurs and these stresses are not relieved because the temperature is relatively low. The compressive layer achieved in ion exchange strengthening is very thin, typically between 10 and 100 μm , with compressive stresses on the order of 300 to 400 MPa, depending on the exchange conditions and glass composition¹¹. Figure 1, adapted from Nordberg¹⁶, illustrates the effect of ‘stuffing’ larger potassium ions into spaces originally occupied by smaller sodium ions.

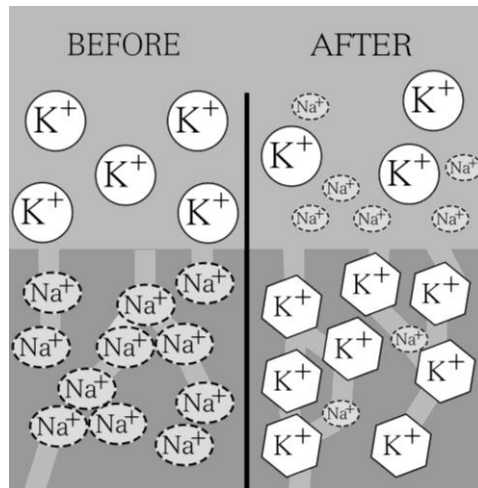


Figure 1. Simplified schematic of the stuffing effect observed in low temperature K^+ for Na^+ ion exchange.

The ion exchange process is governed by the inter-diffusion of sodium and potassium ions from high concentration areas to low concentration areas. Therefore, free sodium ions in the glass diffuse out into the potassium nitrate bath, while potassium ions diffuse into the glass in their stead. This exchange can be described using the following equation:

$$J = -D \frac{dc}{dx} \quad (4)$$

which is Fick's first law of diffusion where J is the flux, D is the inter-diffusion coefficient, and dc/dx is the concentration gradient. The minus sign indicates that mass transfers in the direction of decreasing concentration¹². The rate-limiting step in this inter-diffusion is the transfer rate of the slower moving ion. Because one ion diffuses more slowly, a positive charge differential builds up and creates an electrical potential in addition to the chemical potential from the concentration gradient. This electrical potential causes the slower moving ion to be sped up and the faster moving ion to be slowed down, thereby preserving electrical neutrality¹⁹. The effective diffusion coefficient for an ideal solution can then be summarized as:

$$\bar{D} = \frac{D_A D_B}{\bar{N}_A D_A + \bar{N}_B D_B} \quad (5)$$

where the A and B subscripts represent the two ions being exchanged, \bar{D} is the effective diffusion coefficient, D_A and D_B are the diffusion coefficients for ions A and B, and \bar{N}_A and \bar{N}_B are the mole fractions of ions A and B respectively. Bartholomew¹⁹ goes on to state that because there is temperature dependence between the inter-diffusion and self-diffusion coefficients, the relationship follows the Arrhenius equation:

$$D = D_0 \exp\left(\frac{-E_a}{RT}\right) \quad (6)$$

where D is the diffusion coefficient, D_0 is a temperature independent pre-exponential factor, E_a is the activation energy for inter-diffusion, R is the gas constant, and T is temperature.

C. Fatigue and Lifetime Predictability

The experimental conditions in the LBNE present a unique set of problems regarding the strength and durability of the glass used for PMTs. It has been shown that

under a constant load over time, the strength of a glass deteriorates when exposed to atmospheric water^{20,21}. This phenomenon is known as static fatigue. The mechanism that causes the strength to deteriorate is described by the stress-enhanced reaction of water with the lattice at the crack tip as described by the reaction:



This reaction results in a sharpening of the crack tip and crack growth at a sub-critical crack velocity¹¹. Although not explored in this thesis, chemical strengthening via ion exchange processes has been shown to lessen the effects of static fatigue in silicate glasses²².

Complete immersion in water can have an even more dramatic weakening effect on glass; strengths measured under water can be as much as 20% lower than those measured under normal laboratory conditions²³. This magnitude of strength reduction must be understood and designed for in order to have success in the LBNE.

Crack velocity and its relationship to stress intensity factor, K_I , are important factors to consider when developing lifetime predictions for a glass. This relationship is often expressed in terms of a power law:

$$V = AK_I^n \quad (8)$$

where V is the crack velocity, K_I is the stress intensity, and A and n are constants. The n is the stress-corrosion susceptibility coefficient and ranges between 12 and 35 for most glasses¹². The most direct way to predict the lifetime of a glass under constant stress takes advantage of this relationship. Sub-critical crack velocity causes crack growth, so integrating a crack velocity versus K_I curve at the applied stress intensity results in a time-to-failure value. By integrating in small increments of time and calculating for small amounts of crack growth at each step, the predicted lifetime will be the time at which the length of the crack reaches the thickness of the sample.

Lifetime may also be predicted using a number of other methods, given different available information. If time-to-failure is known at some constant applied stress, then a prediction may be made for other constant applied stresses using the equation:

$$\log t_f = -n \log \sigma_a + C \quad (9)$$

where t_f is the time to failure, σ_a is the applied stress, and C is a constant calculated for a given material. Proof testing can also be used for predicting lifetime; if a specimen survives a test at the proof stress then the stress intensity factor at the crack tip of the strength limiting flaw is known to be less than the critical stress intensity factor. A minimum time-to-failure prediction can then be made using the formula:

$$t_{min} = \frac{2\left(\frac{\sigma_p}{\sigma_a}\right)^{n-2}}{K_{Ic}^{n-2}\sigma_a^2AY^2(n-2)} \quad (10)$$

where σ_p is the proof stress, σ_a is the applied stress, K_{Ic} is the critical stress intensity, and Y is a geometry parameter regarding the shape of the crack tip. The minimum time-to-failure is directly influenced by the ratio of the proof stress to the application stress, the higher the proof stress survived, the longer the predicted lifetime¹².

EXPERIMENTAL PROCEDURE, PART 1: ION EXCHANGE

A. Glass Composition Properties Examined

1. Glass Compositions

The two vendor-supplied glasses used in this experiment share similarities in composition; both are borosilicate glasses with various levels of alkali modifiers. The glass compositions for both vendor glasses fall in the following ranges, given in weight percent in Table I.

Table I. Nominal Composition Ranges for Vendor Glasses in Weight Percent

Oxide	SiO ₂	Na ₂ O	Al ₂ O ₃	ZnO	BaO	CaO	B ₂ O ₃	Li ₂ O
Weight %	60-70	6-9	4-7	0-3	1-4	0-3	15-18	0-3

Using the SciGlass (SciMatics, Newton, MA, USA) database, a number of material properties were predicted for each glass composition to use as a starting point for sample handling. These predictions are presented in Table II. All properties were calculated using A. I. Priven (2000) glass property models²⁴.

Table II. Predicted Glass Properties for the Given Compositions, Acquired from SciGlass Database

Composition	Density (g/cm ³)	Young's Modulus (GPa)	Poisson's Ratio	T _g (°C)	Strain Point (°C)
Vendor 1	2.345	71.68	0.1998	577.4	531.7
Vendor 2	2.453	75.28	0.2025	577.1	531.4

2. Differential Scanning Calorimetry

Small samples of each vendor glass were tested using differential scanning calorimetry (DSC) to determine the glass transition temperature and estimate an

appropriate annealing schedule. The DSC model 2910 (TA Instruments, New Castle, DE, USA) was programmed to heat each sample at a rate of 10°C per minute from room temperature to 610°C under a nitrogen atmosphere. Small shards of sample glass were held in platinum pans tested alongside an empty pan acting as a standard. The glass transition temperatures were estimated using the tangent intercept method on the temperature versus heat flow graph generated by the DSC.

B. Sample Preparation

1. Rod Samples

The two vendor glass compositions were received as cullet and needed to be re-melted in order to create samples for testing. The first samples required were rods suitable for flexural strength testing. In order to create rods, the glasses were melted in a large platinum crucible in a high-temperature furnace. The heating schedule was to increase temperature at a ramp rate of approximately 100°C per hour from 1000°C to 1450°C, then allow the glass to fine for about eight hours. Only large pieces of cullet were used in the melt in order to limit bubble formation in the melted glass. The melted glass was cast in a cylindrical graphite mold, having a 6.4 cm inner diameter and 7.0 cm height. The glass cylinders were annealed for one hour at 550°C to relieve stresses formed during pouring. Alfred University artists were recruited to hand-draw the glass into suitable rods using a technique called cane pulling (Figure 2). The rods created varied in diameter between about 3 and 6 mm because of the nature of the process. This variation is accounted for in the calculation of modulus of rupture (MOR).



Figure 2. Artists Jeff Rowland (left) and Shaun Griffiths (right) in the hot glass shop pulling cane from one of the vendor glasses.

After the cane pulling procedure, the samples were broken into pieces approximately 20 cm long and annealed again using the same schedule in order to relieve residual stresses produced during this process.

2. Disc Samples

Disc samples, for use in hardness testing and UV-Vis spectrometry, were prepared using similar techniques for melting; however, the casting was done in a smaller, steel mold with a 3.2 cm inner diameter and 6.0 cm height. These small glass cylinders were also annealed after casting. Thin discs, approximately 2-4 mm thick, were cut from the cylinders using a large diamond saw (Struers Discotom-5 Cutting Saw, Cleveland, OH, USA). Grinding and polishing of the samples was carried out to achieve a flat, near-optical-quality surface for testing using an 8 inch grinding wheel (Struers DAP-V, Cleveland, OH, USA). Samples were ground by hand on both sides using Si-C paper and constant water flow. Grinding was done with 240-grit Si-C paper to remove burrs left over from cutting, followed by 320-grit, 400-grit, 600-grit, and finally 800 grit paper with average Si-C grain sizes of approximately 63 μm , 41 μm , 26 μm , 15 μm , and 7 μm , respectively.

Following grinding with 800-grit Si-C paper, samples were polished using diamond suspension sprays and polishing pads (MetLab Corporation, Niagara Falls, NY,

USA). The sprays used diamond particle sizes of 6 μm , 3 μm , and 1 μm . Polishing was done with each spray, starting with the largest diamond size and working down. Samples were polished for approximately 3-5 minutes per side, reapplying diamond spray as needed and moving the sample around the polishing wheel, opposite the direction of rotation. Between polishing steps the samples were cleaned with ethanol, and different polishing pads were used for each diamond particle size. After polishing, all samples were wrapped and stored in a desiccator to protect the surface finish before experimentation.

C. Sodium-Potassium Ion Exchange

The ion exchange technique used in this thesis consisted of immersion of the samples in a molten potassium nitrate (KNO_3) bath. Samples of each vendor glass were treated at two different temperatures, 470°C and 480°C, for a dwell period of 24 hours, selected based on results from Hausrath²⁵. Samples were arranged in a specially designed apparatus using two vertically aligned pieces of stainless steel mesh and a baseplate, which allowed the rods to be treated while upright, exposing the length of the rods to the surrounding molten salt. Disc samples were held similarly, using a narrower stainless steel mesh, shaped specifically for the task of exposing the surface to the salt bath. After treatment was completed, the holding apparatus was removed from the bath and allowed to cool to room temperature, at which point samples and holders were rinsed with water to dissolve excess salt deposits on the glass surface. The samples were stored in a desiccator to protect the surface treatments.

D. Evaluating K^+ Exchange Depth

In order to explore the depth of exchange accomplished in the two glasses using the different treatment schedules, electron microprobe (JEOL JXA-8200, Tokyo, Japan) mapping of elements was performed on cross-sections of rod samples. Sixteen total rods, eight of each vendor glass, four of each ion exchange treatment, were selected to calculate an average exchange depth of K^+ . The samples were cut into short lengths after the ion exchange bath and mounted vertically in epoxy. The epoxy mounts and sample surfaces were then ground and polished down to 1 μm diamond polish using the same

techniques described above in Section B. 2. Once polished, samples were given a conductive sputter coating to facilitate microprobe testing.

A microprobe map was created for each rod by aligning the beam approximately with the interface of the glass with the epoxy mount. Data was collected along 10 rows perpendicular to the sample edge, spaced $4\ \mu\text{m}$ apart. The measurements were made at $2\ \mu\text{m}$ intervals along the row (Figure 3). Silicon, sodium, and potassium levels were tracked from the edge of the sample up to approximately $50\ \mu\text{m}$ depth.

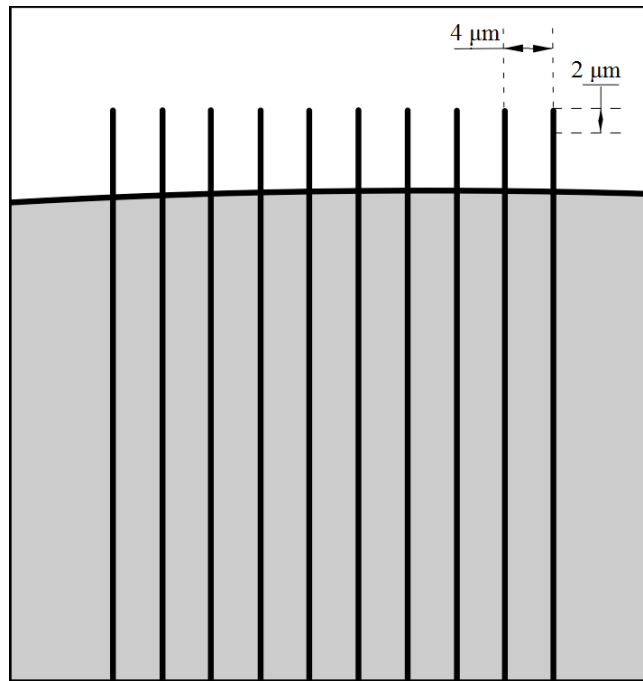


Figure 3. Diagram of microprobe mapping. The gray area represents the glass sample and the white represents the epoxy mount. The vertical lines indicate paths along which measurements were conducted.

E. Flexural Strength Measurement

The strength of the two vendor glasses was determined using four-point bend flexural testing. Rod samples were broken into lengths of approximately 50 mm and separated into groups according to vendor composition and exchange treatment. Thirty untreated samples of each vendor glass and 15 samples of each ion exchange schedule for each glass were selected for flexural strength testing. The diameter of the samples was measured in three places prior to testing to ensure limited variation along the length of each rod and to calculate an average diameter.

The custom-made four-point bend testing apparatus (Figure 4) features four steel cylinders perpendicular to the test sample to allow the load to settle in the x direction, two above and two below, resulting in contact at four points along the rod. Below the two support rods another steel cylinder runs lengthwise through the holder to offer freedom of movement in the z direction, and below that a steel beam reinforces the plastic body of the part. The apparatus also features a point contact in the form of a steel ball bearing above the support span, which allows for 360 degree articulation during load application. The loading span of the test setup is 20 mm while the support span is 40 mm.

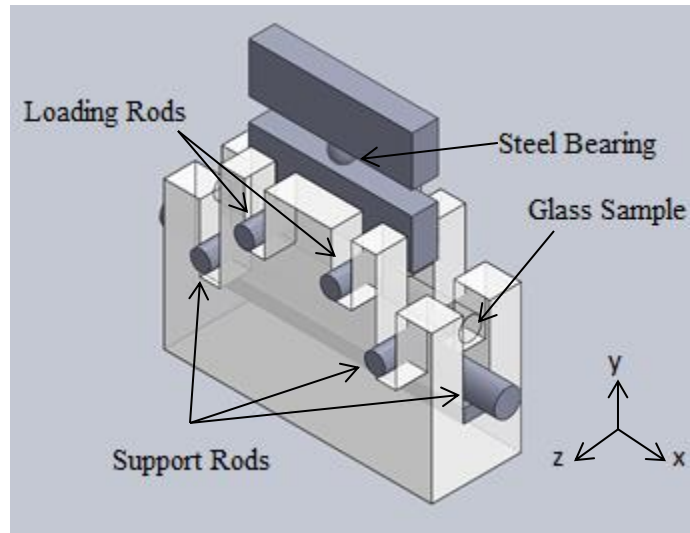


Figure 4. Schematic of 4-point bend testing apparatus with important elements and axes labeled.

All samples were tested using a crosshead speed of 0.5 mm/min and data was collected at 10 points/second. The load applied at the time of failure was used to calculate modulus of rupture (MOR) for each sample using the following equation²⁶:

$$\text{MOR} = \frac{5.09La}{d^3} \quad (11)$$

where L is the breaking load in Newtons, a is the separation between adjacent support and loading edges in millimeters, and d is the average diameter of the sample in millimeters.

F. Surface Hardness

Surface hardness of the disc samples was investigated in order to provide a comparison between surface effects of ion exchange strengthening and bulk effects (MOR). A Shimadzu HMV-2000 micro-indenter (Shimadzu Corporation, Kyoto, Japan) was used to measure Vickers hardness of the polished disc samples both before and after ion exchange treatment. Four loads were applied during testing; 200, 300, 500, and 1000 g. Twenty individual measurements were made at each load, with each sample held under load for 15 seconds.

The Vickers hardness number (H_V) was automatically calculated for each indentation using the following equation¹²:

$$H_V = \frac{1.8544F}{d^2} \quad (12)$$

where F is the applied load in kg and d is the average length of the two diagonals in millimeters. An overall average hardness and standard deviation were calculated for each set of measurements made at constant load.

G. UV-Vis Spectroscopy

In order to show that the ion exchange treatments did not significantly increase the absorbance properties of the glass between 350 and 500 nm, disc samples were tested using a Lambda 950 Spectrophotometer (Perkin-Elmer, Shelton, CT, USA) both before and after ion exchange treatment. The samples were cleaned with ethanol immediately before testing to eliminate any surface contamination and ensure a good measurement. These wavelengths were chosen because the majority of detectable Cherenkov light falls in this range²⁷; consequently, increases in the absorbance at these wavelengths would be detrimental to the efficacy of the LBNE detector.

EXPERIMENTAL PROCEDURE, PART 2: CRACK VELOCITY

A. Residual Stress Analysis

Residual stresses from the formation of PMTs could lead to reduced overall strength performance of bulbs and affect crack velocity upon failure. Residual stress analysis was performed by Rudolph Instruments (Denville, NJ). Two Vendor 1 PMT bulbs were examined using an AP-07 Digital Polariscope (Rudolph Instruments, Denville, NJ, USA) at a wavelength of 630 nm. The refractive index of the bulbs was determined to be 1.4917, with slight variations across the surface due to the manufacturing process. Using this value, the PMT was surrounded by an immersion liquid matching the refractive index of the glass to facilitate polariscope measurements. The results of this stress analysis revealed significant surface and axial stresses in the glass, ranging up to 25 MPa²⁸. Tensile stresses of this magnitude could significantly weaken the integrity of the PMT and cause failure at reduced external pressure.

B. Pressure Testing

BNL has conducted prototypic tests concerning the reliability of standard Vendor 1 PMTs under hydrostatic pressure at the Naval Undersea Warfare Center (NUWC) in Newport, RI. In these tests, PMTs were secured near the center of a 15-meter diameter, spherical steel tank, and submerged in filtered water. The tank was pressurized using an air pump, up to 0.61 MPa at the center of the vessel and failure was induced by impact of a steel bolt plunger. The primary objective of these tests was to observe and measure the pressure wave following a bulb failure. Once fracture initiated during testing, the complete fragmentation of the bulb lasted only a few milliseconds, as water filled the volume that was previously under vacuum. The inward rush of water stopped upon impact of the water on itself, thus creating a shockwave moving outward⁸.

Following the preliminary shockwave tests at the NUWC, a series of implosion tests were conducted at BNL with the primary objective of inducing and observing the failure of PMT bulbs under hydrostatic pressure. The testing procedure was such that PMT specimens would be subjected to a pressure rise from zero to 300 psi over a time

span of five minutes, two hours, or 24 hours. Pressurization was controlled using LabVIEW (National Instruments, Austin, TX, USA) software to ensure consistent rates of loading and to record the pressure at failure of each PMT. Each test and failure was recorded using a high-speed camera, filming at speeds of 4,000-6,000 frames per second, in order to capture, in detail, the mode and progression of failure in each specimen. These high speed recordings allow us to follow the growth of cracks in the bulb surface and measure crack velocity under real world conditions.

C. Crack Velocity Measurement

Analysis of high-speed videos taken at BNL began with the identification of failure origins and resolution of measurable cracks. Each test recording was examined frame-by-frame in order to measure the propagation of individual cracks along the surface of the sample. Measured cracks were selected based on visibility and traceable propagation through several frames of video. Once selected, on-screen propagation distances were measured by identifying the crack tip in the earliest possible frame and marking the spot with masking tape. The video was then advanced by a single frame, the new position of the crack tip was marked, and the distance from the original mark was then recorded. This procedure was repeated throughout all measurable frames to obtain a total distance of crack propagation (Figure 5). Scaling factors were determined for each individual video using the known diameter of the bulbs (10 inches) as compared to the measured, on-screen diameter. Multiplying the as-measured distances by the scaling factor of the bulb in question gave real total distances for crack propagation.

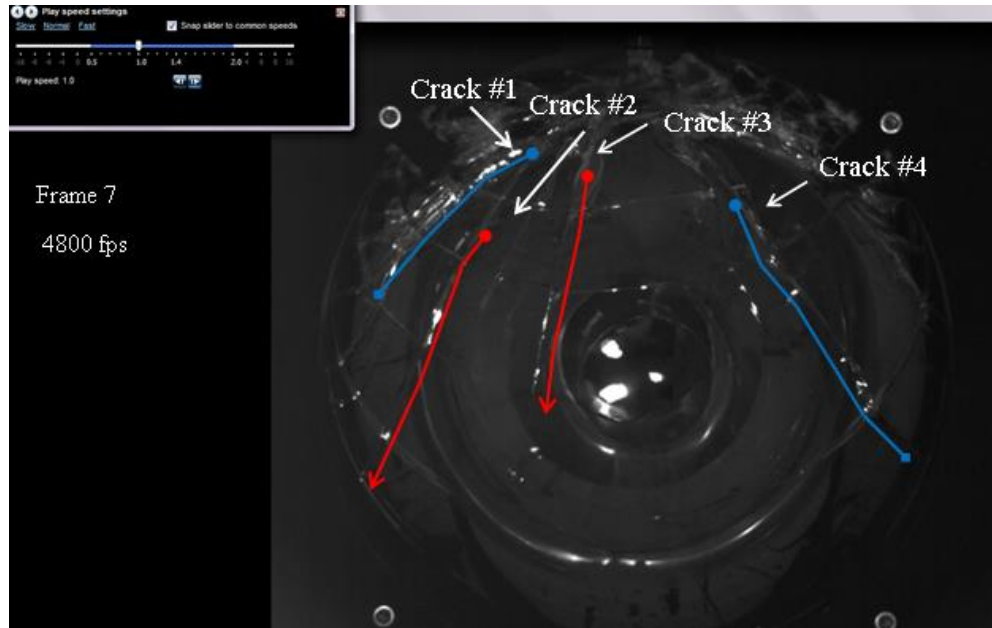


Figure 5. Example of a single frame used for crack measurement, the bulb is being viewed from the top down. Cracks indicated with red are being measured in the current frame in the direction of the arrow. Measurements have been completed on cracks indicated in blue.

The number of frames measured during crack growth gives a time value for velocity calculations when multiplied by the frame rate of the given video. Crack velocity was calculated for individual cracks and an average velocity was found for all measurable cracks on each specimen using the scaled propagation distances and time values. A sample calculation of crack velocity is given in the appendix in Table IX.

Although this method of measurement yielded valid results, it only accounted for the crack propagation in two dimensions in the video frame. The curvature of the bulb increases the actual crack length relative to the measured length. Therefore the actual crack velocity is expected to be higher than the initially calculated values.

D. 3-D Modeling and Curvature Corrections

In order to correct the initial crack velocities, a 3-D computer model of a 10-inch Vendor 1 PMT bulb, developed at BNL, was used as a projection surface for the crack distances measured from the implosion recordings. Two-dimensional measurements of

the crack path were transferred into SolidWorks (Dassault Systèmes, Vélizy-Villacoublay, France) modeling software by measuring crack tip positions in each frame of video and using the center peak of the bulb as a reference point. By noting the distance from the bulb peak and an angle from vertical, the crack tip positions could be accurately transferred to the corresponding position on the bulb model. These positions were sketched into the computer-aided design (CAD) drawing in the form of rays radiating from the reference point on a plane perpendicular to the bulb peak (Figure 6). Connecting the outer ends of the rays gave a representation of the total crack path, which was then projected onto the surface of the model, giving curvature of the crack itself (Figure 7). The arc lengths of the new, curved paths were measured using the built-in measure tool in SolidWorks. The arc lengths were used to calculate corrected crack velocities for each individual crack, as well as averages for each PMT, and an overall average for all samples.

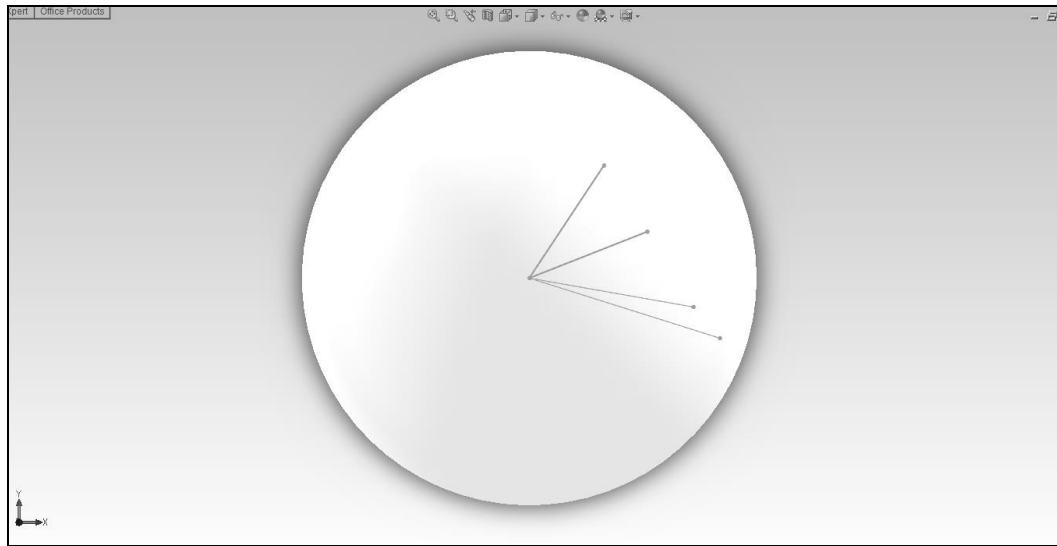


Figure 6. A top-down view of the bulb model, each line segment represents a measurement point along the crack path, relative to the central peak of the bulb.

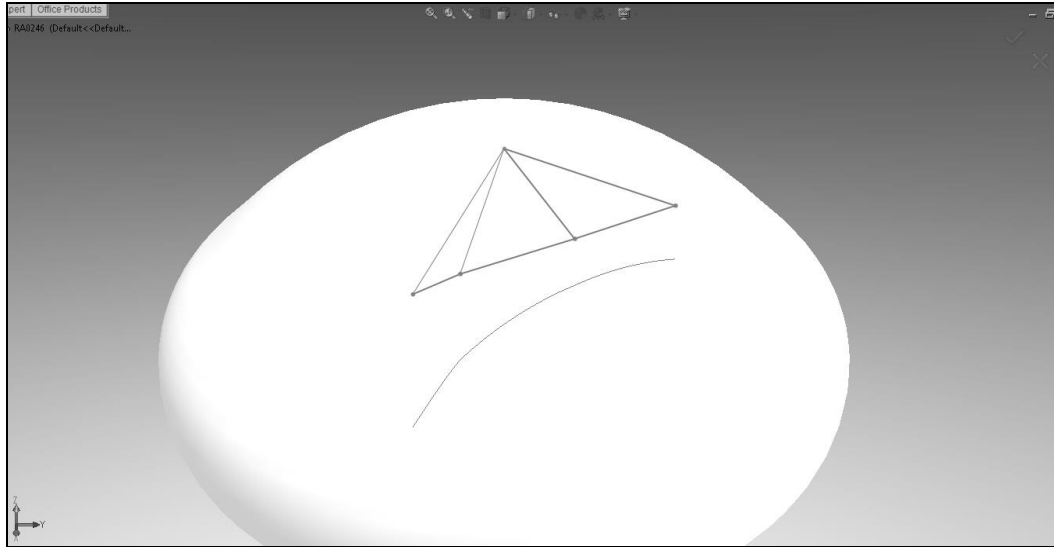


Figure 7. In a rotated view of the bulb model, the segments from Figure 6 are visible, in dark gray, connected at their ends by the 2-dimensional representation of the crack path. The light gray arc below represents the intersection of the projection of the 2-D path and the bulb surface.

RESULTS

A. Differential Scanning Calorimetry

DSC measurements give an approximate measure of the glass transition temperature by plotting heat flow as a function of temperature. Using the slope intercept method the glass transition temperature (T_g) of the two glasses were determined to be 510°C for Vendor 1 and 540°C for Vendor 2. Figure 8 and Figure 9 show the plots and the slope-intercept estimation of the glass transition for the two glasses. These estimates were used as the basis for choosing annealing schedules for the glasses throughout this work.

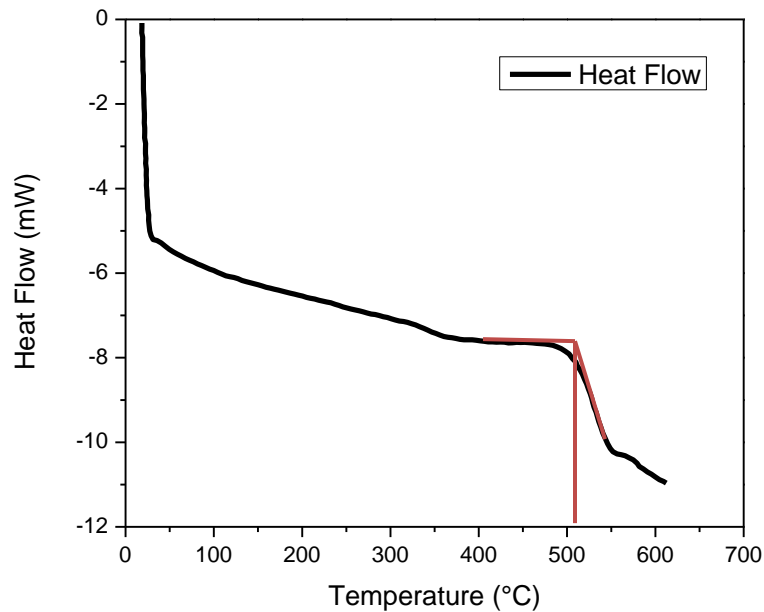


Figure 8. Heat flow vs. temperature curve of Vendor 1 composition using a heating rate of 10°C per minute with T_g estimated at 510°C.

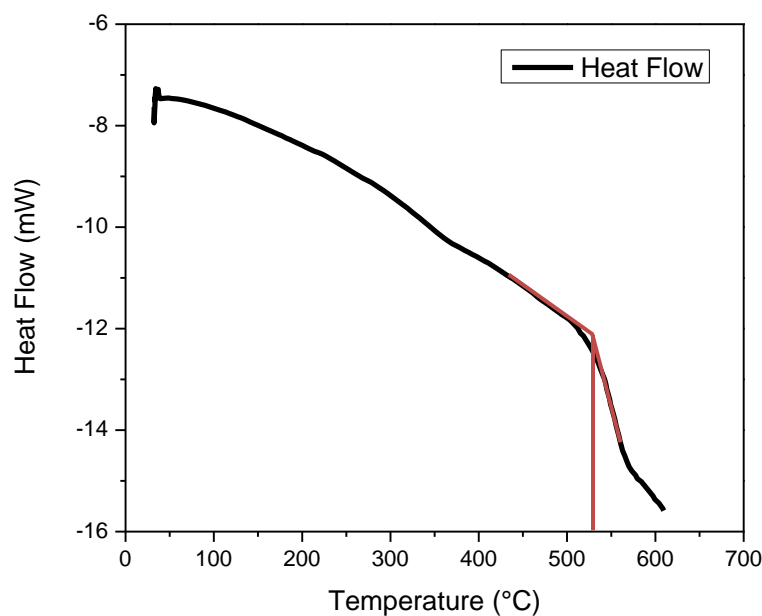


Figure 9. Heat flow vs. temperature curve of Vendor 2 composition using a heating rate of 10°C per minute with T_g estimated at 540°C.

B. Depth and Profile of K^+ Exchange

The exchange profile of potassium for each ion exchange treatment was measured using electron microprobe mapping. In each case, similar exchange depths and profiles were achieved. Higher temperature treatments on both glasses resulted in increased maximum concentrations of potassium ions at the sample surface. For each treatment, four samples were measured and an average profile was created, plotting intensity vs. depth. In order to determine depth the sample edge was estimated in the data using silicon intensity as a marker. The first relevant data point (0 μm depth) was assumed to be the first point where silicon intensity reached more than half of its maximum intensity value. Figure 10 shows the measured intensity of the three elements as a function of the depth for Vendor 1 glass treated at 470°C for 24 hrs. The exchange depth for these conditions was estimated to be about 28 μm . The maximum K^+ intensity was 2708 counts at 4 μm . Figure 11, Figure 12, and Figure 13 show intensity versus depth for Vendor 1 glass treated

at 480°C for 24 hours, Vendor 2 glass treated at 470°C and 480°C for 24 hours, respectively. Table III summarizes the important points of each graph.

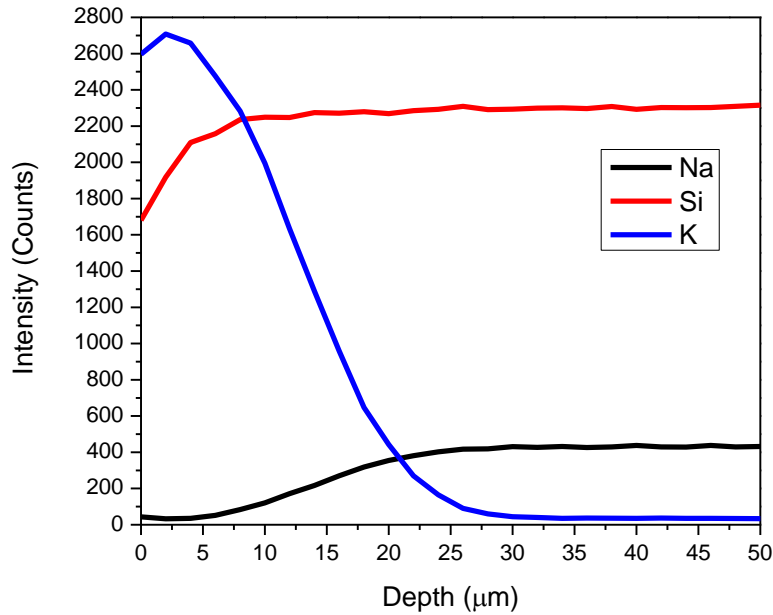


Figure 10. Exchange profile of Vendor 1 glass treated at 470°C for 24 hours.

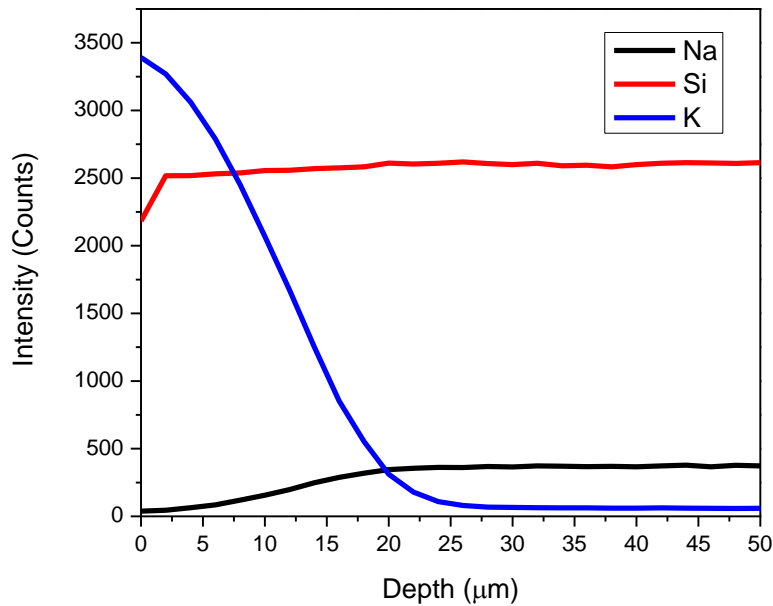


Figure 11. Exchange profile of Vendor 1 glass treated at 480°C for 24 hours.

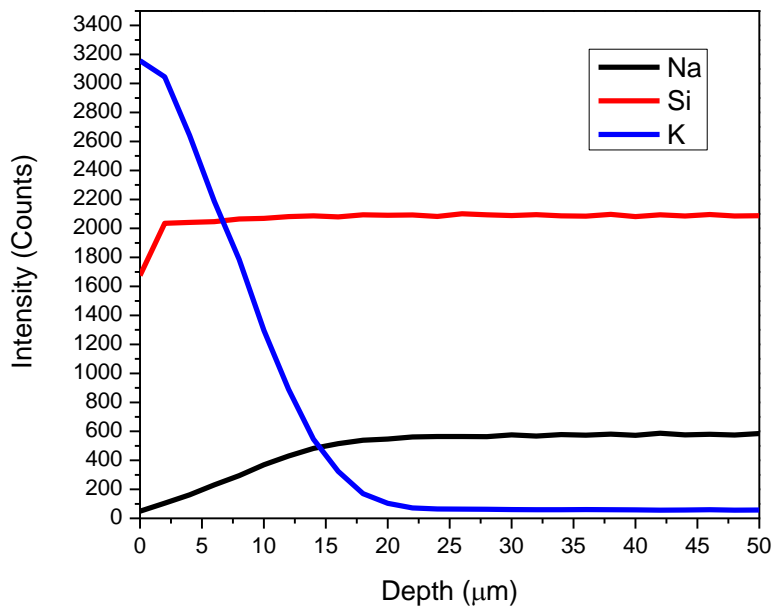


Figure 12. Exchange profile of Vendor 2 glass treated at 470°C for 24 hours.

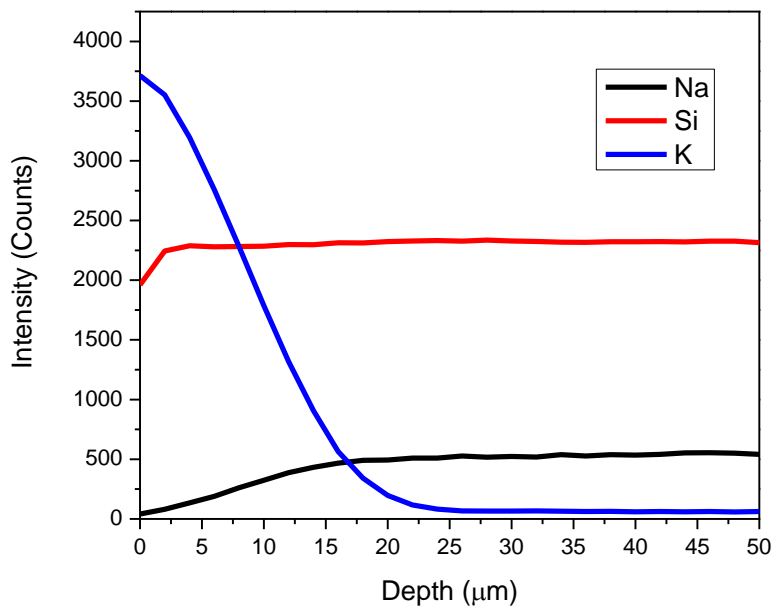


Figure 13. Exchange profile of Vendor 2 glass treated at 480°C for 24 hours.

Table III. Summary of Ion Exchange Profile Results

Glass Composition	Exchange Treatment	Exchange Depth (μm)	Maximum $\text{K}^+:\text{Si}$ Ratio
Vendor 1	470°C, 24 h	28	1.75
	480°C, 24 h	28	1.55
Vendor 2	470°C, 24 h	22	1.89
	480°C, 24 h	26	1.89

C. Flexural Strength

In order to determine the effectiveness of the ion exchange treatments, examination of the change in strength between the untreated glass and the strengthened glass was performed. The glass strengths were tested using a 4-point bend tensile test. Simple average values of MOR measured for the two glasses were calculated and are compiled in Table IV.

Table IV. Average Modulus of Rupture and Standard Deviation for Vendor Glasses

Glass Composition	Exchange Treatment	Average MOR (MPa)	Standard Deviation (MPa)
Vendor 1	None	133.96	28.00
	470°C, 24 h	197.62	34.66
	480°C, 24 h	192.83	22.45
Vendor 2	None	156.43	37.56
	470°C, 24 h	247.56	52.80
	480°C, 24 h	201.42	50.40

The MOR of Vendor 1 glass increased by 48% when treated at 470°C, and by 44% when treated at 480°C. Vendor 2 glass results show a 58% increase in strength with the 470°C treatment and a 29% increase after the 480°C treatment.

Weibull distributions of MOR were created for each glass and ion exchange treatment (Figure 14 and Figure 15). By applying linear regression to the failure data for

each glass treatment, characteristic strength was calculated. Characteristic strength is defined as the strength at which there is a 63.2% probability of failure of a given sample. Table V summarizes the results of Weibull statistics performed on the two glasses in terms of Weibull modulus and characteristic strength.

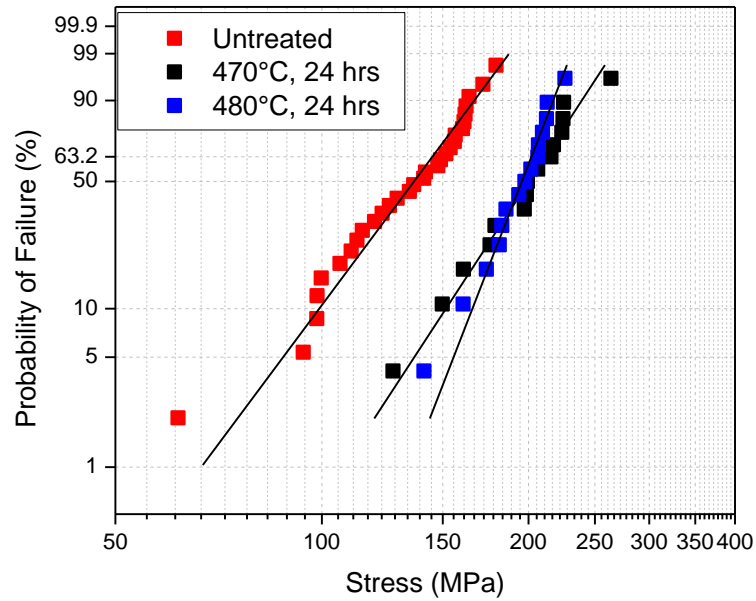


Figure 14. Weibull plot of 4-point bend strength of Vendor 1 glass at various exchange treatments.

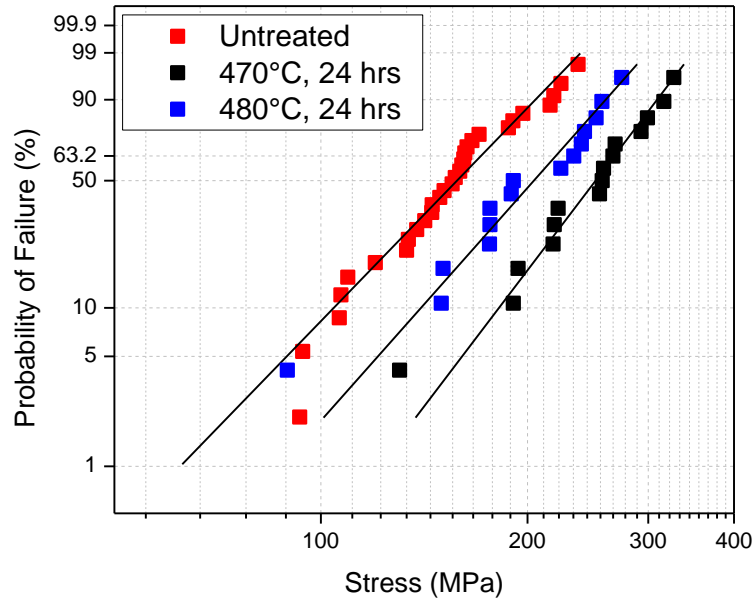


Figure 15. Weibull plot of 4-point bend strength of Vendor 2 glass rods at various exchange treatments.

Table V. Summary of Weibull Modulus and Characteristic Strength Results

Glass Composition	Exchange Treatment	Weibull Modulus	Characteristic Strength (MPa)
Vendor 1	None	5.9	144.8
	470°C, 24 h	6.8	211.5
	480°C, 24 h	11.4	202.0
Vendor 2	None	4.6	171.1
	470°C, 24 h	5.8	267.7
	480°C, 24 h	5.0	219.9

The characteristic strengths give slightly different values for improvement after ion exchange than the simple averages. For Vendor 1 glass treated at 470°C, there is an increase in strength of 46 %, while there was an improvement of 40 % for the 480°C treatment. The Weibull modulus has also improved in both cases compared with the untreated samples. For the Vendor 2 glass there is a strength increase of 57 % after the

470°C treatment and an increase of 29 % after the 480°C treatment. Both treatments also improved the Weibull modulus calculated from the untreated Vendor 2 results.

D. Surface Hardness

The Vickers Hardness of each glass was tested before and after chemical strengthening in order to gauge the surface effects of the process in comparison to the bulk (MOR) effects. Figure 16 and Figure 17 show the hardness results for untreated and treated samples of the two vendor glasses measured at loads between 200 and 1000 g and a hold time of 15 seconds.

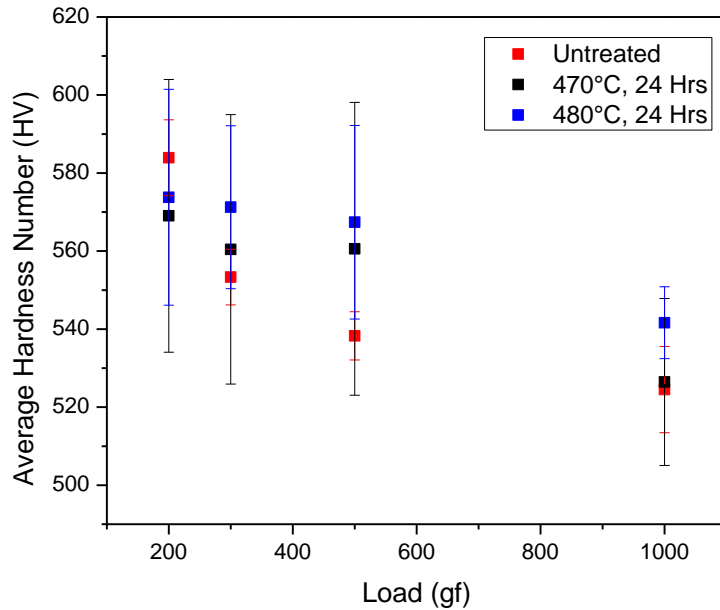


Figure 16. Vickers Hardness of Vendor 1 glass before and after ion exchange.

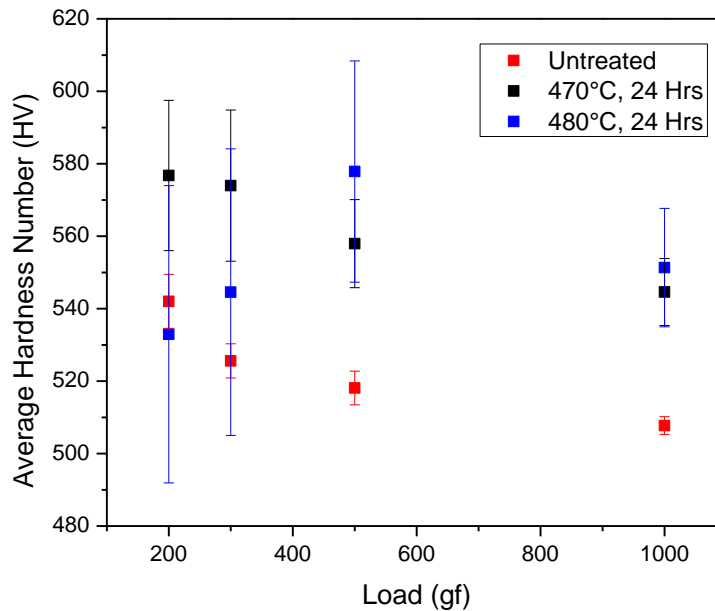


Figure 17. Vickers Hardness of Vendor 2 glass before and after ion exchange.

E. UV-Vis Spectroscopy

Absorbance was measured in two untreated disc samples of each vendor glass in order to obtain a baseline with which to compare the samples after ion exchange. The same samples were then subjected to ion exchange treatment, one sample of each vendor composition at each temperature of salt bath. This allows us to eliminate factors such as inhomogeneity in the glass or thickness of selected samples as factors affecting the absorbance and isolate observed changes due to the added salt compression layer. Figure 18 and Figure 19 illustrate these effects.

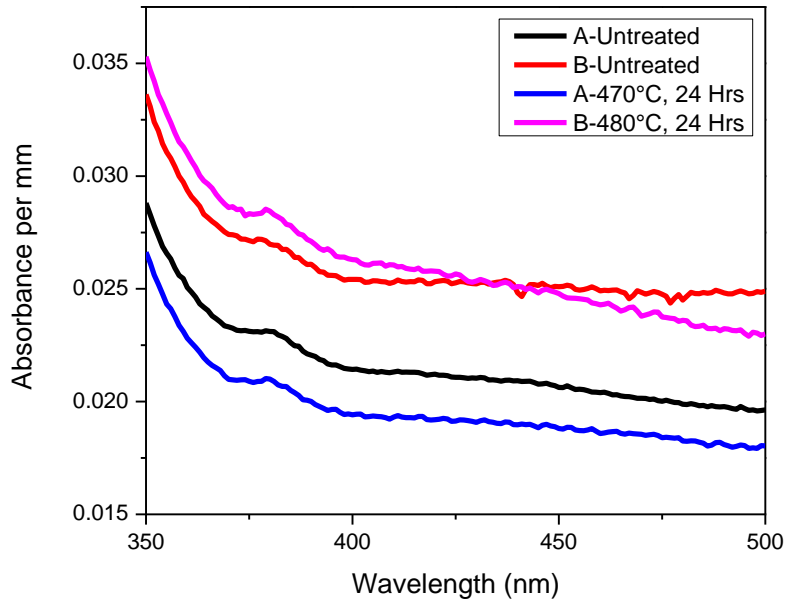


Figure 18. Normalized absorbance of light between 350 and 500 nm wavelengths of Vendor 1 glass samples "A" and "B" before and after exchange.

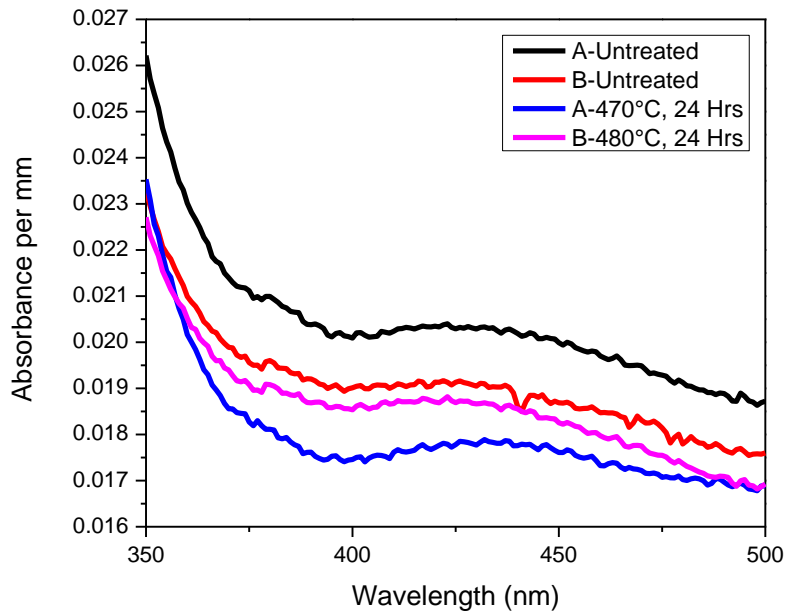


Figure 19. Normalized absorbance of light between 350 and 500 nm wavelengths of Vendor 2 glass samples "A" and "B" before and after exchange.

In order to account for the thickness of the samples used, the absorbance measurements were normalized to a ‘per millimeter’ absorbance. In addition to graphical analyses, the percent change in absorbance across the designated wavelengths was quantitatively determined using the following formula:

$$\% \textit{Difference} = \frac{|A_U - A_T|}{A_U} * 100 \quad (13)$$

where A_U is the normalized absorbance of the untreated sample and A_T is the normalized absorbance of the treated sample. Using this formula, an 8.88 % average decrease is calculated in absorbance per mm between Vendor 1 sample “A” in the treated and untreated states. The same calculation performed on Vendor 1 “B” gives a 3.51 % difference over the range of wavelength. For Vendor 2 sample “A” a 12.12 % decrease is calculated, and a decrease in normalized absorbance of 2.56 % for Vendor 2 sample “B”.

F. Crack Velocity

In all, 32 cracks were measured between nine separate implosion tests performed on Vendor 1 PMTs and an overall average crack velocity was calculated. With the initial method, the average velocity was found to be 205.82 m/s with a standard deviation of 47.49 m/s. When the curvature correction procedure was applied, new values were calculated, giving an average velocity of 231.84 m/s with a standard deviation of 59.04 m/s. The curve correction procedure shows a 13 % increase in the average measured velocity and a 24 % increase in standard deviation. A summary of the results calculated for each bulb, including standard deviation and pressure at failure, is presented in Table VI. The average crack velocities for each bulb using each method were plotted against the external pressure at which the bulb failed in testing (Figure 20).

Table VI. Summary of Crack Velocity Data

Bulb Designation	Pressure at Break (psi)	# of Cracks Measured	Average Crack Velocity with Initial Method (m/s)	Standard Deviation (m/s)	Average Crack Velocity with Curve Correction (m/s)	Standard Deviation (m/s)
RA0246	260	4	191.91	63.70	201.54	71.46
RA0227	269	1	192.26	--	201.00	--
TA3610	205	3	239.20	57.08	251.47	106.53
TA3281	103	5	144.35	36.52	160.06	44.77
TA3522	293.94	4	250.33	132.34	312.53	185.32
TA3598	298.6	6	148.74	30.25	175.11	33.01
TA3624	130.3	3	168.32	15.30	191.93	24.35
TA3410	131.5	3	242.11	109.82	276.42	122.95
TA3479	214.7	3	275.17	101.70	316.51	132.03

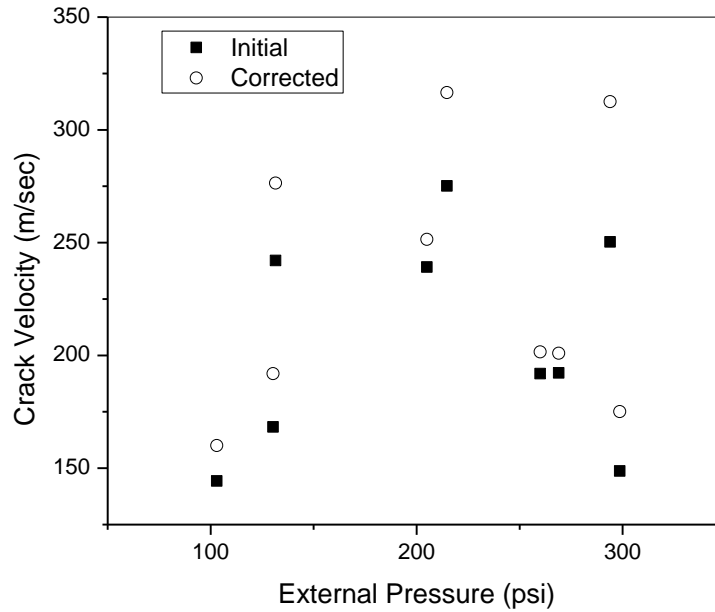


Figure 20. Scatter plot of average crack velocity against external pressure at failure for each bulb using each of the two methods of measurement.

DISCUSSION

A. Ion Exchange Effects on Properties

1. Flexural Strength

The results of the selected ion exchange treatments show significant strength increases over untreated glasses in each case. Table IV shows the simple averages calculated for flexural strength as well as the standard deviation among the samples. Variation of sample diameter was not intentional; it was an artifact of the cane pulling process. In order to account for the statistical nature of glass failures the strength data was plotted in Figure 14 and Figure 15 using a Weibull distribution. These plots, along with Table V, show the relative improvement in strength and Weibull modulus for the two vendor glasses.

Evaluating the effectiveness of the two exchange treatments in Table V reveals that both treatments resulted in similar gains in strength for Vendor 1 glass. However, for Vendor 2 samples, the 480°C treatment produced 18 % lower characteristic strength values than those achieved with the 470°C treatment. This indicates that the extended time of treatment and relative proximity of the temperature to the strain point of the glasses has resulted in some stress relaxation. The strain point is the temperature at which the glass viscosity is $10^{14.6}$ Poise²⁹ and represents the lower end of the glass transformation range at which internal stresses in the glass are released over the course of several hours¹². The closeness of the treatment temperature to the strain point allows for some release of the compressive stress layer formed over the 24 h exchange time, resulting in lower measured strength. The relaxation affects all four testing arrangements; flexural strengths of ion exchanged glasses can reach in excess of 100 % increases over untreated glasses²⁵. The treatment schedules used are not ideal for the given compositions. In order to optimize the treatment schedules for the two glasses a much more extensive range of temperature and time variation needs to be explored.

2. Indentation Hardness

Indentation hardness measurements were performed in order to compare the effects of ion exchange to those observed in the flexural strength results. The flexural strength is a property of the bulk glass, whereas indentation hardness is measured at the surface. Increased indentation hardness in the surface of PMTs could help reduce the severity of surface damage caused during handling and placement within the detector system.

Figure 16 shows the measured hardness of the Vendor 1 glass at four different loads in the treated and untreated states. There is no increase in hardness for either exchange process when accounting for error in the measurements. However, in Figure 17, the behavior of the Vendor 2 glass does not follow the same trend. There is a measurable increase in hardness after the 470°C treatment over the entire range of indentation loads. The 480°C measurements do not show an increase in hardness at low loading; however, the hardness does increase appreciably at the 500 and 1000 g loads. Relaxation behavior during the exchange treatments explains the trends observed in both glasses. The Vendor 1 glass, which has a lower T_g , experiences relaxation at both exchange temperatures, resulting in similar hardness number values to the untreated glass. Vendor 2, which has a higher T_g , shows increased hardness at all loads for the lower temperature exchange. In the case of the higher exchange temperature, the relaxation of surface stresses results in similar hardness measurements to untreated glass when measured at low loads. The remaining compressive stress gives increased hardness at the greater depths reached with higher indentation loads.

3. Absorbance

After determining that ion exchange treatment could improve the strength and hardness of the glasses being used for PMTs, it was important to ensure that such treatment would not negatively impact the optical performance of the glass. In order to determine the effect of ion exchange on the transmission of Cherenkov light, the spectroscopic properties of both available glasses were evaluated before and after ion exchange. The same glass disc was tested before and after a treatment to eliminate some variability in the measurements.

The testing range of 350-500 nm wavelengths was selected in order to encompass the majority of wavelengths where Cherenkov radiation is detected. In the normalized absorbance plots of Vendor 1 and Vendor 2 samples, Figure 18 and Figure 19, respectively, there are no significant changes in the features of the spectra or increases in absorbance.

The observed differences in absorbance between untreated samples of the same composition can be attributed to a number of factors including possible inhomogeneity in the melt as well as differences in the quality of the surface polish. Although there is an apparent reduction in absorbance due to ion exchange in each case, the difference between the untreated samples is of a similar magnitude; thus making it impossible to say with certainty that the differences in absorbance were caused solely by the strengthening procedure.

B. Crack Velocity and Modeling

The curvature correction procedure results in increased standard deviation in the crack velocities measured. Increased deviation is due in part to variation in the degree of curvature of the PMT surface along different crack paths. Cracks occurring around the outer radius of the bulb are subject to much greater degree of curvature than those moving across the upper surface. Therefore, the velocity measurements are affected to different degrees. The crack velocities measured using this video recording method are well below reported terminal crack velocity of reference glasses measured by other means, summarized in Table VII³⁰. This low velocity trend was not expected, given the circumstances of the PMT failure. Being completely submerged in water and highly pressurized, it was hypothesized that the crack velocities would measure higher than typical accepted values.

Table VII. Terminal Crack Velocities for Various Reference Glasses³⁰

Material	Terminal Crack Velocity (m/s)
Soda Lime Glass	1460-1600
Mirror Glass	1520
Borosilicate Crown Glass (BK-7)	1677-1800
Fused Silica	2100-2500

There are other factors that may partially account for the reduction in crack velocity. It is likely that the residual tensile stresses in the surface of the PMTs tested by Rudolph Instruments are systematic to all bulbs processed in the same way. These residual tensile stresses may counteract the external compressive, hydrostatic force, mitigating any crack velocity increase that would have stemmed from the pressure at failure. The layered structure of the PMT, also reported by Rudolph, could be responsible for impeding crack propagation through the bulb, further reducing the observed crack velocity. Additionally, the thermal history of the PMT bulbs dictates flaw population and distribution and thus stress concentration at different sections of the PMT. Filming speed of a maximum of 6,000 frames per second limits the ability to record faster events. Nevertheless, this approach to crack velocity measurement is unique in that the crack propagation can be observed *in situ* and measured as it progresses in real time.

The data collected does not reveal any direct correlation between the external pressure of testing and the average crack velocity for each bulb. However, it is possible that individual cracks, due to location on the bulb surface, are subjected to additional stress in different sections of the PMT because of its shape. In PMT TA3522, an equatorial crack is measured at nearly twice the velocity of the other cracks measured on the bulb (Figure 21, Table VIII). This is consistent with pressure modeling performed at BNL, which shows a ring of increased stress around the circumference of a 10-inch bulb under pressure (Figure 22). This correlation indicates that the stress model is accurate

and directly impacts the failure of the bulbs. The same increased crack velocity near the high stress band is observed in two other implosion sample bulbs; TA3410 and TA3479. Because the stress intensity factor in the exact region of the cracks at failure cannot be measured *in situ*, the effect on crack velocity cannot be quantified using this method.

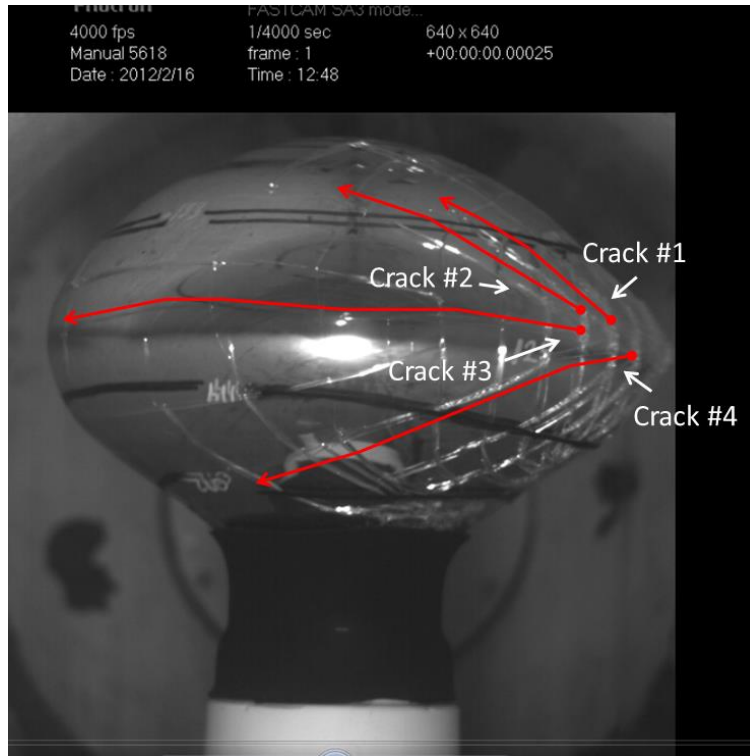


Figure 21. Individual frame of video showing the location of cracks measured on PMT TA3522.

Table VIII. Crack Velocities Measured in TA3522 After Curvature Correction

Crack Number	Measured Velocity
	(m/s)
Crack #1	134.27
Crack #2	253.00
Crack #3	571.84
Crack #4	290.99

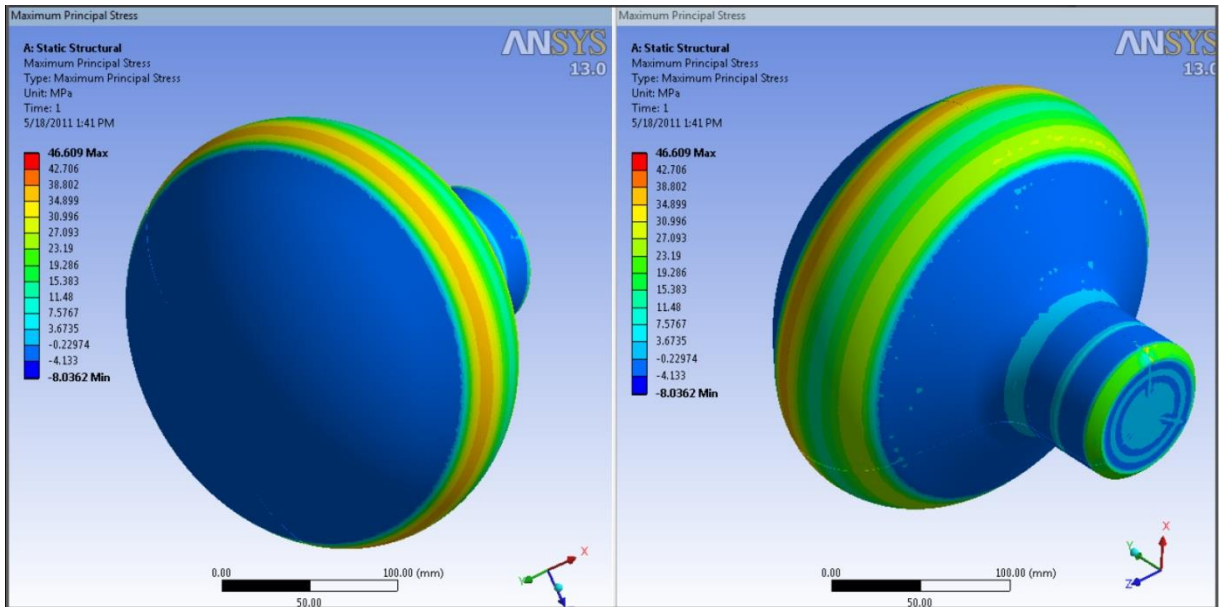


Figure 22. CAD model of a 10-inch PMT showing the maximum principal stresses under uniform hydrostatic pressure.

SUMMARY AND CONCLUSIONS

A. Ion Exchange

Results from this work indicate that the two vendor glasses exceed the requirements of the LBNE project for strength. However, these results do not correlate directly to the as-formed PMT glasses. If ion exchange treatment could be added to the preparation of bulbs for the LBNE, it would add a factor of safety to the lifetime of PMTs over the course of the project. Results of testing showed measurably improved flexural strength in both vendor glasses and increased surface hardness in one even using non-ideal exchange schedules. The appearance of stress relaxation phenomena in both glasses during long time exchanges emphasizes the need to optimize the ion exchange process in order to obtain the best possible results for both strength and hardness. The results of UV-Vis spectroscopy indicate that there would be no significant difference in the optical properties of the glasses with ion exchange treatment. All the testing completed in this work indicates that ion exchange strengthening would have a positive impact on the reliability of PMTs in the LBNE project over its lifetime.

B. Crack Velocity

Results show crack velocities measured using the high speed video method are well below expected terminal crack propagation velocities. The low crack velocities measured are attributed to a number of possible factors, including residual stresses in the glass that depends on the thermal history, the layered structure of Vendor 1 PMTs, and limitations to the method including video resolution and filming speed reducing visibility of the crack tip. This novel method of observation still gives us important information about the nature of the failure of PMT bulbs under hydrostatic pressure. Under ideal circumstances, this method could provide precise crack propagation data for *in situ* PMT bulb fractures. Understanding the nature of the failure with regards to the effect of residual stress and internal glass structure is a continuing goal.

FUTURE WORK

In order to build on the basis covered in this thesis and provide a complete picture of the probable lifetime of PMTs in the LBNE, more exhaustive testing needs to be conducted. A detailed analysis of static fatigue effects in the vendor glasses when in contact with high purity water is important to formulating a lifetime prediction for the glasses in service. This testing would result in understanding of the effect of leaching, as well as slow crack growth on the strength and durability of the given glasses. Lifetime prediction could also be achieved by constructing a Weibull distribution of MOR vs. loading rate to calculate the probability of survival at a given time.

In order to implement ion exchange as a step in the preparation, an ideal exchange treatment needs to be determined by varying the temperature, time, and exchange methods used. In addition, there may be glass compositions that are better suited for the task, specifically compositions with high strength and chemical durability. Compositional space needs to be investigated.

REFERENCES

1. J. N. Bahcall, "Solving the Mystery of the Missing Neutrinos" (2004) NobelPrize.org. Accessed on: February, 2014. Available at <http://www.nobelprize.org/nobel_prizes/themes/physics/bahcall>
2. R. Davis, D. Harmer, and K. Hoffman, "Search for Neutrinos from the Sun," *Phys. Rev. Lett.*, **20** [21] 1205-9 (1968).
3. J. Boger, R. L. Hahn, J. K. Rowley, A. L. Carter, B. Hollebhone, D. Kessler, I. Blevins, F. Dalnoki-Veress, A. Dekok, J. Farine, D. R. Grant, C. K. Hargrove, G. Laberge, I. Levine, K. McFarlane, H. Mes, A. T. Noble, V. M. Novikov, M. O'Neill, M. Shatkay, C. Shewchuk, D. Sinclair, E. T. H. Clifford, R. Deal, E. D. Earle, E. Gaudette, G. Milton, B. Sur, J. Bigu, J. H. M. Cowan, D. L. Cluff, E. D. Hallman, R. U. Haq, J. Hewett, J. G. Hykawy, G. Jonkmans, R. Michaud, A. Roberge, J. Roberts, E. Saettler, M. H. Schwendener, H. Seifert, D. Sweezey, R. Tafirout, C. J. Virtue, D. N. Beck, Y. D. Chan, X. Chen, M. R. Dragowsky, F. W. Dycus, J. Gonzalez, M. C. P. Isaac, Y. Kajiyama, G. W. Koehler, K. T. Lesko, M. C. Moebus, E. B. Norman, C. E. Okada, A. W. P. Poon, P. Purgalis, A. Schuelke, A. R. Smith, R. G. Stokstad, S. Turner, I. Zliven, J. M. Anaya, T. J. Bowles, S. J. Brice, E.-I. Esch, M. M. Fowler, A. Goldschmidt, A. Hime, A. F. McGirt, G. G. Miller, W. A. Teasdale, J. B. Wilhelmy, J. M. Wouters, J. D. Anglin, M. Bercovitch, W. F. Davidson, R. S. Storey, S. Biller, R. A. Black, R. J. Boardman, M. G. Bowler, J. Cameron, B. Cleveland, A. P. Ferraris, G. Doucas, H. Heron, C. Howard, N. A. Jelley, A. B. Knox, M. Lay, W. Locke, J. Lyon, S. Majerus, M. Moorhead, M. Omori, N. W. Tanner, R. K. Taplin, M. Thorman, D. L. Wark, N. West, J. C. Barton, P. T. Trent, R. Kouzes, M. M. Lowry, A. L. Bell, and E. Bonvin, "The Sudbury Neutrino Observatory," *Nucl. Instrum. Methods Phys. Res., Sect. A*, **449** [1-2] 172-207 (2000).
4. S. Fukuda, Y. Fukuda, T. Hayakawa, E. Ichihara, M. Ishitsuka, Y. Itow, T. Kajita, J. Kameda, K. Kaneyuki, S. Kasuga, K. Kobayashi, Y. Kobayashi, Y. Koshio, M. Miura, S. Moriyama, M. Nakahata, S. Nakayama, T. Namba, Y. Obayashi, A. Okada, M. Oketa, K. Okumura, T. Oyabu, N. Sakurai, M. Shiozawa, Y. Suzuki, Y. Takeuchi, T. Toshito, Y. Totsuka, S. Yamada, S. Desai, M. Earl, J. T. Hong, E. Kearns, M. Masuzawa, M. D. Messier, J. L. Stone, L. R. Sulak, C. W. Walter, W. Wang, K. Scholberg, T. Barszczak, D. Casper, D. W. Liu, W. Gajewski, P. G. Halverson, J. Hsu, W. R. Kropp, S. Mine, L. R. Price, F. Reines, M. Smy, H. W. Sobel, M. R. Vagins, K. S. Ganezer, W. E. Keig, R. W. Ellsworth, S. Tasaka, J. W. Flanagan, A. Kibayashi, J. G. Learned, S. Matsuno, V. J. Stenger, Y. Hayato, T. Ishii, A. Ichikawa, J. Kanzaki, T. Kobayashi, T. Maruyama, K. Nakamura, Y. Oyama, A. Sakai, M. Sakuda, O. Sasaki, S. Echigo, T. Iwashita, M. Kohama, A. T. Suzuki, M. Hasegawa, T. Inagaki, I. Kato, H. Maesaka, T. Nakaya, K. Nishikawa, S. Yamamoto, T. J. Haines, B. K. Kim, R. Sanford, R. Svoboda, E.

- Blaufuss, M. L. Chen, Z. Conner, J. A. Goodman, E. Guillian, G. W. Sullivan, D. Turcan, A. Habig, M. Ackerman, F. Goebel, J. Hill, C. K. Jung, T. Kato, D. Kerr, M. Malek, K. Martens, C. Mauger, C. McGrew, E. Sharkey, B. Viren, C. Yanagisawa, W. Doki, S. Inaba, K. Ito, M. Kirisawa, M. Kitaguchi, C. Mitsuda, K. Miyano, C. Saji, M. Takahata, M. Takahashi, K. Higuchi, Y. Kajiyama, A. Kusano, Y. Nagashima, K. Nitta, M. Takita, T. Yamaguchi, M. Yoshida, H. I. Kim, S. B. Kim, J. Yoo, H. Okazawa, and M. Etoh, "The Super-Kamiokande Detector," *Nucl. Instrum. Methods Phys. Res., Sect. A*, **501** [2-3] 418-62 (2003).
5. K. Abe, T. Abe, H. Aihara, Y. Fukuda, Y. Hayato, K. Huang, A. K. Ichikawa, M. Ikeda, K. Inoue, H. Ishino, Y. Itow, T. Kajita, J. Kameda, Y. Kishimoto, M. Koga, Y. Koshio, K. P. Lee, A. Minamino, M. Miura, S. Moriyama, M. Nakahata, K. Nakamura, T. Nakaya, S. Nakayama, K. Nishijima, Y. Nishimura, Y. Obayashi, K. Okumura, M. Sakuda, H. Sekiya, M. Shiozawa, A. T. Suzuki, Y. Suzuki, A. Takeda, Y. Takeuchi, H. K. M. Tanaka, S. Tasaka, T. Tomura, M. R. Vagins, J. Wang, and M. Yokoyama, "Letter of Intent: The Hyper-Kamiokande Experiment- Detector Design and Physics Potential" (2011) Cornell University. Accessed on: February, 2014. Available at <<http://arxiv.org/abs/1109.3262>>
 6. V. Barger, M. Bishai, D. Bogert, C. Bromberg, A. Curioni, M. Dierckxsens, M. Diwan, F. Dufour, D. Finley, B. T. Fleming, J. Gallardo, J. Heim, P. Huber, C. K. Jung, S. Kahn, E. Kearns, H. Kirk, T. Kirk, K. Lande, C. Laughton, W. Y. Lee, K. Lesko, C. Lewis, P. Litchfield, A. K. Mann, A. Marchionni, W. Marciano, D. Marfatia, A. D. Marino, M. Marshak, S. Menary, K. McDonald, M. Messier, W. Pariseau, Z. Parsa, S. Pordes, R. Potenza, R. Rameika, N. Saoulidou, N. Simos, R. V. Berg, B. Viren, K. Whisnant, R. Wilson, W. Winter, C. Yanagisawa, F. Yumiceva, E. D. Zimmerman, and R. Zwaska, "Report of the U.S. Long Baseline Neutrino Experiment Study" (2007) Cornell University. Accessed on: February, 2014. Available at <<http://arxiv.org/pdf/0705.4396v1.pdf>>
 7. J. Goon and I. Stancu, "The Long-Baseline Neutrino Experiment Conceptual Design Report" (2012) Cornell University. Accessed on: February, 2014. Available at <<http://arxiv.org/abs/1204.2295>>
 8. M. Diwan, J. Dolph, J. Ling, T. Russo, R. Sharma, K. Sexton, N. Simos, J. Stewart, H. Tanaka, D. Arnold, P. Tabor, and S. Turner, "Underwater Implosions of Large Format Photo-Multiplier Tubes," *Nucl. Instrum. Methods Phys. Res., Sect. A*, **670**, 61-7 (2012).
 9. E. Orowan, *Z. Krist.*, **A89**, 327-343 (1934). As Cited in A. K. Varshneya, *Fundamentals of Inorganic Glasses*, 3rd ed.; p. 451. Academic Press, Boston, MA, 2006.
 10. W. C. LaCourse, "Strength of Glass"; pp. 451-512 in *Introduction to Glass Science*. Edited by L. D. Pye, H. J. Stevens, and W. C. LaCourse. Plenum Press, NY, 1972.

11. J. E. Shelby, *Introduction to Glass Science and Technology*, 2nd ed. The Royal Society of Chemistry, Cambridge, UK, 2005.
12. A. K. Varshneya, *Fundamentals of Inorganic Glasses*, 3rd ed. Academic Press, Boston, MA, 2006.
13. B. Proctor, "The Effects of Hydrofluoric Acid Etching on the Strength of Glass," *Phys. Chem. Glasses*, **3** [1] 7-27 (1962).
14. R. E. Armstrong, Union Carbide Corporation, "Armstrong Method for Fire Polishing," US Patent 3188190, June 8, 1965.
15. R. Gardon, "Thermal Tempering of Glass"; pp. 145-216 in *Glass Science and Technology, Vol. 5, Elasticity and Strength in Glasses*. Edited by D. R. Uhlmann and N. J. Kreidl. Academic Press, New York, 1980.
16. M. E. Nordberg, E. L. Mochel, H. M. Garfinkel, and J. S. Olcott, "Strengthening by Ion Exchange," *J. Am. Ceram. Soc.*, **47** [5] 215-9 (1964).
17. G. Partridge and P. W. McMillan, "Strengthening of Glass by Surface Crystallization," *Glass Technol.*, **15** [5] 127-33 (1974).
18. D. A. Duke, J. E. Megles, J. F. MacDowell, and H. F. Bopp, "Strengthening of Glass-Ceramics by Application of Compressive Glazes," *J. Am. Ceram. Soc.*, **51** [2] 98-101 (1968).
19. R. F. Bartholomew and H. M. Garfinkel, "Chemical Strengthening of Glass"; pp. 217-70 in *Glass Science and Technology, Vol. 5, Elasticity and Strength in Glasses*. Edited by D. R. Uhlmann and N. J. Kreidl. Academic Press, New York, 1980.
20. R. E. Mould and R. D. Southwick, "Strength and Static Fatigue of Abraded Glass under Controlled Ambient Conditions, Pt. 1," *J. Am. Ceram. Soc.*, **42** [11] 542-7 (1959).
21. R. E. Mould and R. D. Southwick, "Strength and Static Fatigue of Abraded Glass under Controlled Ambient Conditions, Pt. 2," *J. Am. Ceram. Soc.*, **42** [12] 582-92 (1959).
22. V. M. Sglavo, A. Prezzi, and T. Zandonella, "Engineered Stress-Profile Silicate Glass: High Strength Material Insensitive to Surface Defects and Fatigue," *Adv. Eng. Mater.*, **6** [5] 344-9 (2004).
23. T. C. Baker and F. W. Preston, "The Effect of Water on the Strength of Glass," *J. Appl. Phys.*, **17** [3] 179-88 (1946).

24. A. I. Priven, "General Method for Calculating the Properties of Oxide Glasses and Glass-Forming Melts from Their Composition and Temperature," *Glass Technol.*, **45** [6] 244-54 (2004).
25. R. L. Hausrath, "Investigation into the Effect of Salt Composition on the Short-Time Ion Exchange Strengthening of Soda-Lime Silicate Glass"; M.S. Thesis. Alfred University, Alfred, NY, 2008.
26. "Standard Test Methods for Strength of Glass by Flexure," ASTM Designation C158-02. American Society for Testing and Materials, West Consohocken, PA.
27. J. A. Aguilar, A. Albert, P. Amram, M. Anghinolfi, G. Anton, S. Anvarf, F. E. Ardellier-Desages, E. Aslanides, J.-J. Aubert, R. Azoulay, D. Bailey, S. Basa, M. Battaglieri, Y. Becherini, R. Bellotti, J. Beltramelli, V. Bertin, M. Billault, R. Blaes, F. Blanc, R. W. Bland, N. d. Botton, J. Boulesteix, M. C. Bouwhuis, C. B. Brooks, S. M. Bradbury, R. Bruijn, J. Brunner, F. Bugeon, G. F. Burgio, F. Cafagna, A. Calzas, L. Caponetto, E. Carmona, J. Carr, S. L. Cartwright, S. Cecchini, P. Charvis, M. Circella, C. Colnard, C. Compère, J. Croquette, S. Cooper, P. Coyle, S. Cuneo, G. Damy, R. v. Dantzig, A. Deschamps, C. D. Marzo, J.-J. Destelle, R. D. Vita, B. Dinkelspiler, G. Dispau, J.-F. Drougou, F. Druillole, J. Engelen, S. Favard, F. Feinstein, S. Ferry, D. Festy, J. Fopma, J.-L. Fuda, J.-M. Gallone, G. Giacomelli, N. Girard, P. Goret, J.-F. Gournay, G. Hallewell, B. Hartmann, A. Heijboer, Y. Hello, J. J. Hernández-Rey, G. Herrouin, J. Höbl, C. Hoffmann, J. R. Hubbard, M. Jaquet, M. d. Jong, F. Jouvenot, A. Kappes, T. Karg, S. Karkar, M. Karolak, U. Katz, P. Keller, P. Kooijman, E. V. Korolkova, A. Kouchner, W. Kretschmer, V. A. Kudryavtsev, H. Lafoux, P. Lagier, P. Lamare, J.-C. Languillat, L. Laubier, T. Legou, Y. L. Guen, H. L. Provost, A. L. V. Suu, L. L. Nigro, D. L. Presti, S. Loucatos, F. Louis, V. Lyashuk, P. Magnier, M. Marcelin, A. Margiotta, C. Maron, A. Massol, F. Mazéas, B. Mazeau, A. Mazure, J. E. McMillan, J.-L. Michel, C. Millot, A. Milovanovic, F. Montanet, T. Montaruli, J.-P. Morel, L. Moscoso, E. Nezri, V. Niess, and G. J. Nooren, "Transmission of Light in Deep Sea Water at the Site of the Antares Neutrino Telescope," *Astropart. Phys.*, **23** [1] 131-55 (2005).
28. M. Diwan, Brookhaven National Laboratory, Upton, NY, January, 2013, Private Communication.
29. R. H. Doremus, *Glass Science*, 2nd ed. John Wiley, New York, 1994.
30. G. Quinn, "Fractography of Ceramics and Glasses" (2007) National Institute of Standards and Technology. Accessed on: February, 2014. Available at <www.nist.gov/customcf/get_pdf.cfm?pub_id=850928>

APPENDIX

Table IX. Sample Calculation of Crack Velocity

Crack #1	Δ length measured (cm)	Scale Factor	Δ length actual (cm)
Frame 1-2	2.95	1.454	4.29
Frame 2-3	1.84	1.454	2.68
Frame 3-4	1.54	1.454	2.24
			Total = 9.20

Frame Rate 4000 fps \rightarrow 3 frames = $3/4000$ s

Average Velocity = (Total Δ Length)/Time = $9.2 \text{ cm}/(3/4000 \text{ s}) = 12271.76 \text{ cm/s}$